

***Final Draft***  
**of the original manuscript:**

Hakimizad, A.; Raeissi, K.; Golozar, M.A.; Lu, X.; Blawert, C.;  
Zheludkevich, M.L.:

**The effect of pulse waveforms on surface morphology,  
composition and corrosion behavior of Al<sub>2</sub>O<sub>3</sub> and Al<sub>2</sub>O<sub>3</sub>/TiO<sub>2</sub>  
nano-composite PEO coatings on 7075 aluminum alloy**

In: Surface and Coatings Technology (2017) Elsevier

DOI: [10.1016/j.surfcoat.2017.05.068](https://doi.org/10.1016/j.surfcoat.2017.05.068)

**The effect of pulse waveforms on surface morphology, composition and corrosion behavior of Al<sub>2</sub>O<sub>3</sub> and Al<sub>2</sub>O<sub>3</sub>/TiO<sub>2</sub> nano-composite PEO coatings on 7075 aluminum alloy**

Amin Hakimizad<sup>1,\*</sup>, Keyvan Raeissi<sup>1</sup>, Mohammad Ali Golozar<sup>1</sup>, Xiaopeng Lu<sup>2,3</sup>, Carsten Blawert<sup>2</sup>, Mikhail L. Zheludkevich<sup>2</sup>

<sup>1</sup> Department of Materials Engineering, Isfahan University of Technology, Isfahan 84156–83111, Iran

<sup>2</sup> Institute of Materials Research, Helmholtz-Zentrum Geesthacht, Max-Planck-Str. 1, Geesthacht, 21502, Germany

<sup>3</sup> Key Laboratory for Anisotropy and Texture of Materials, Education Ministry of China, School of Material Science and Engineering, Northeastern University, 3-11 Wenhua Road, Shenyang 110819, China

(\* Corresponding author, E-mail: a.hakimizad@ma.iut.ac.ir)

**Abstract**

Plasma electrolytic oxidation was employed to produce Al<sub>2</sub>O<sub>3</sub> and Al<sub>2</sub>O<sub>3</sub>/TiO<sub>2</sub> composite coatings from a silicate based electrolyte on 7075 aluminum alloy using unipolar and bipolar waveforms with cathodic duty cycle of 20 and 40 %. The results showed that the surface morphology of the coatings is dependent on the applied waveform. Pancake like morphology was converted to crater like by altering waveform from unipolar to bipolar. Higher thickness, lower porosity, and thus, higher corrosion protection were achieved using the bipolar waveform at higher cathodic duty cycle of 40 %. The incorporation of TiO<sub>2</sub> nano-particles in the coatings

decreased the thickness, increased the **micro-cracks** and widened the **micro-pores** on coating surface when unipolar waveform was applied. It was found that TiO<sub>2</sub> **nano-particles** have been incorporated into the coatings in their original crystalline structure, i.e. rutile, which was categorized in the “inert incorporation” mode and this incorporation has not changed the matrix **micro-structure**, i.e.  $\gamma$ -alumina. In addition, the incorporated amounts of TiO<sub>2</sub> **nano-particles** were constant and showed no reasonable relation with the applied waveform. The corrosion results indicated that although the composite coating produced at unipolar waveform shows the highest corrosion resistance at short periods of immersion due to repairing mechanism, it degrades at a higher rate. However, for the composite coatings produced using the bipolar waveform with the higher cathodic duty cycle of 40 %, the maximum corrosion protection was achieved at long term immersion. Repairing mechanism is plugging the **micro-pores** in the inner compact layer which was found more effective for the coatings with lower porosity. Accordingly, it was concluded that the corrosion protection of the coatings with higher “intrinsic resistance” get more benefit from the repairing mechanism too.

**Keywords:** plasma electrolytic oxidation; composite coatings; surface morphology; corrosion; pulse waveforms; titania **nano-particle**.

## **1. Introduction**

Plasma electrolytic oxidation (PEO), also known as micro arc oxidation (MAO) or anodic spark deposition (ASD) [1] is an anodizing process assisted by plasma discharges for producing oxide films on surface of valve metals and light alloys. **PEO is usually used for metals such as titanium, magnesium, tantalum, zirconium, aluminum and their alloys** [2-7], which provide stable oxides in aqueous media [8-10]. Compared to vacuum based plasma processes, PEO has

been preferred for its non-line-of-sight treatment and atmospheric working environment [11]. This technology has evolved from conventional anodizing, but the electrolytes used are different and it demands much higher voltages to maintain dielectric breakdown of the anodic oxide film, which is featured by a number of discrete short-lived **micro-discharges** moving across the metal surface. As a result, PEO coatings are normally much thicker [10]. Such oxide layers show controllable morphology and composition, excellent bonding strength with substrate, good electrical and thermal properties, high **micro-hardness** and suitable wear and corrosion resistance [12].

PEO process can be carried out using direct current (DC), alternating current (AC) or pulsed DC regimes [13]. DC power supplies with high output voltages have been used widely, but the produced layers are thin, porous and typically show low adhesion to the substrate. On the other hand, a pulsed DC with a high peak current gives rise to additional polarization on electrode surface by building up a charged double layer, thus unipolar produced coatings would still be porous. However, the application of unbalanced AC power supply with non-similar positive and negative voltages provides a wide possibility to control the coating composition and **micro-structure**. In this case, the coating possesses lower porosity, higher adhesion to the substrate, and is thoroughly different from the coating produced by DC or unipolar pulsed DC power supplies [14]. However, the main disadvantages of AC process are low coating growth rates, the presence of a relatively thick porous outer layer (which must be removed later at the finishing stages of the manufacturing process) and low energy efficiency [15]. Moreover, the results show that the pulsed bi-polar current (PBC) regime acts better than a DC or low frequency AC regime [13]. It seems that the frequency range of 1 to 3 kHz provides adequate conditions for fast and energy-efficient formation of oxide layers on aluminum alloys using a PBC mode [15].

Unfortunately, the discharges create not only the coating, but also some defects, for example discharge channels, pores from gas inclusions and cracks [16]. Thus, sealing or avoidance of the high porosity is essential to improve the coating properties. Particle addition into PEO coatings is a novel approach to obtain a type of in situ sealing [17]. Examples of such particles in PEO coatings include silica and lanthanum oxide [17-20], silicon nitride [16], clay [21] and titanium dioxide [22]. The incorporation of **nano-particles** in the oxide layer structure improves its tribological [23] and corrosion [24] behavior, and also, increases its hardness and adhesion to the substrate [25]. Many industries such as machinery, textile and printing are interested on Al<sub>2</sub>O<sub>3</sub>/TiO<sub>2</sub> composite coatings due to their high hardness, excellent wear and corrosion properties, as well as high thermal and chemical resistance [26]. Li et al. [27] have reported higher hardness and adhesion of PEO coatings on 6063 Al alloy by the presence of TiO<sub>2</sub> **nano-particles** in electrolyte bath. Particles can incorporate in coating formation either inertly like Si<sub>3</sub>N<sub>4</sub> [16] or reactively like clay [21] depending on the size and melting point of the particles as well as the treatment conditions [17, 18]. Anatase peaks **have been** reported visible for all the particle-containing coatings, indicating that the particles are inertly incorporated into the PEO layer of Magnesium alloy although it **is** found dependent on coating conditions [22]. Our previous work revealed that adding TiO<sub>2</sub> **nano-particles** into a silicate based electrolyte has reduced the porosity of PEO oxide layers produced by a DC process, independent of their concentration [28]. In the present study, the effects of waveform (unipolar and bipolar) on structure and corrosion properties of Al<sub>2</sub>O<sub>3</sub> and Al<sub>2</sub>O<sub>3</sub>/TiO<sub>2</sub> composite coatings created on 7075 aluminum alloy are investigated.

## 2. Experimental

### 2.1. Sample preparation

20 mm × 12 mm (Ø\*H) cylindrical pieces of 7075 aluminum with the chemical composition shown in Table 1 were used as the substrate specimens. The circumferences of the specimens were masked using epoxy adhesive and thermal shrink. Thus, only two flat sides of the cylindrical specimen were available for oxidation. The flat surfaces of all specimens were polished down to an average roughness of 0.08 μm using SiC abrasive paper, and after degreasing in an acetone charged ultrasonic cleaner and rinsing in deionized water, the samples were dried in the warm air blow. Prepared specimens were then directly transferred to the coating bath.

### 2.2. Plasma electrolytic oxidation

PEO process was carried out in 66 L of a silicate base electrolyte consisting of 10 g L<sup>-1</sup> Na<sub>2</sub>SiO<sub>3</sub> and 2 g L<sup>-1</sup> KOH (called S1). The same electrolyte containing additional 3 g L<sup>-1</sup> TiO<sub>2</sub> **nano-particles** (rutile in spherical shape with average diameter of 30 nm) (called S2) was used for producing composite coatings. The electrolyte bath was continuously stirred using a centrifugal pump operating at 160 L min<sup>-1</sup>. The temperature of the electrolyte was kept constant at 25±1°C using a digital thermostat controller (stainless steel thermocouple placed directly in the electrolyte) and an industrial reciprocal compressor chiller. The samples were coated using three different waveforms of unipolar and bipolar types with cathodic duty cycle of 20 and 40 %. All the waveforms were applied for 1 h at 2 kHz frequency with average anodic (positive) current density of 5.6 A/dm<sup>2</sup>. A rectifier with a maximum output of 750 V/30 A equipped with an additional Isolated Gate Bipolar Transistor (IGBT) based pulse converter was used as the power supply. During the PEO processes, potential-time responses were recorded and a GPS 2024

digital oscilloscope was used to monitor the waveforms. The recorded waveforms are shown in Figure 1. The bath compositions, sample codes and visual appearance of the coatings are represented in Table 2. Each sample was connected to a double shielded copper wire used as working electrode (anode). Two 30 cm × 30 cm 316 L stainless steel sheets were used as counter electrodes (cathodes) placed at both sides of the working specimens in order to overcome the “*shelter effect*” [11] and ensuring the same quality of coatings obtained on both sides of the specimens.

### 2.3. Characterization

The thicknesses of the coatings were measured using an eddy current coating thickness gauge (model CEM DT-156); ten random measurements were taken from each coated surface followed by a statistical analysis to calculate the mean thickness value and standard variations [29]. Surface roughness was evaluated using a profilometer (model Mitotoyo SurfTest stylus working on standard of ISO 1997).

The phase composition of the samples was evaluated by means of a glancing angle X-Ray diffractometer (GAXRD, Bruker X-ray diffractometer). The X-ray diffraction scan was measured over a  $2\theta$  range of 20–80 ° using Cu K $\alpha$  radiation generated at 40 kV and 30 mA. The incident angles were 3, 5 and 10 °. X’pert Highscore software with PDF2 database was employed to analyze the XRD patterns. A scanning electron microscope (TESCAN Vega3 SB) combined with an energy dispersive spectrometer (EDS) system from eumeX (IXRFsystems) was used to study the as-received surface morphology and polished cross-sections of the specimens (which were sputtered with a thin gold layer in order to prevent surface charging effects [15]). The cross-sections were ground through successive grades of SiC papers, followed by finishing to 1  $\mu$ m diamond. The surfaces of the samples were analyzed by energy dispersive spectroscopy

(EDS) in order to determine the chemical composition and elemental maps of the coatings. An acceleration voltage of 15 kV was applied for SEM and EDS investigations. SEM (model Philips XL30) was used to study the surfaces of the corroded coatings.

#### 2.4. Evaluation of corrosion behavior

The corrosion tests were performed using an AMETEK potentiostat/galvanostat (model PARSTAT 2273). The tests were carried out in a three electrode cell kit with a standard calomel electrode (SCE) as the reference electrode and a platinum plate as the counter electrode. The corrosion behavior of the coatings was evaluated by potentiodynamic polarization tests after 1 h immersion in 3.5 wt.% NaCl solution at pH 4, adjusted by adding HCl acid solution. The potential scan, which ranged from -250 to 2000 mV versus open circuit potential (OCP) at a scan rate of 1 mV s<sup>-1</sup>, was used for potentiodynamic polarization readings. Based on the approximately linear polarization behavior observed near OCP (around ±50 mV), polarization resistances were calculated from the line slopes and using Stern–Geary equation [5, 30-33]:

$$R_p = \frac{\beta_a \beta_c}{2.303 i_{corr} (\beta_a + \beta_c)} \quad (1)$$

where  $R_p$  is the polarization resistance,  $\beta_a$  and  $\beta_c$  are anodic and cathodic Tafel slopes, respectively, and  $i_{corr}$  is the corrosion current density.

Electrochemical impedance spectroscopy (EIS) was used for further study of corrosion behavior of the coatings especially after long time immersions up to 16 weeks in 3.5 wt. % NaCl solution at pH 4. The frequency range of 100 kHz–100 mHz and 10 mV peak-to-peak voltage amplitude versus OCP were used for the measurements. The EIS data were analyzed using Zview software. In all tests, specimens with 2.54 cm<sup>2</sup> surface area were exposed to the corrosive solution, and each test was repeated at least three times.

**Table 1: Chemical composition of 7075 aluminum alloy used as substrates**

Element	Zn	Mg	Cu	Fe	Si	Cr	Mn	Al
Content	5.1	2.2	1.2	0.3	0.2	0.2	0.2	Balance

(wt%)

**Table 2: The visual appearances and coating conditions of Al<sub>2</sub>O<sub>3</sub> and Al<sub>2</sub>O<sub>3</sub>/TiO<sub>2</sub> composite coatings**

Waveform	Bath 1 (S1)	Bath 2 (S2)
Parameters	10 g L <sup>-1</sup> Na <sub>2</sub> SiO <sub>3</sub> + 2 g L <sup>-1</sup> KOH	10 g L <sup>-1</sup> Na <sub>2</sub> SiO <sub>3</sub> + 2 g L <sup>-1</sup> KOH + 3 g L <sup>-1</sup> TiO <sub>2</sub> <b>nano-particles</b>
Frequency=2 kHz Anodic duty ratio=20% Cathodic duty ratio=0% (W1)	 S1W1	 S2W1
Frequency=2 kHz Anodic duty ratio=20% Cathodic duty ratio=20% (W2)	 S1W2	 S2W2

Frequency=2 kHz  
Anodic duty ratio=20%  
Cathodic duty ratio=40%  
(W3)



S1W3



S2W3

### 3. Results and discussion

#### 3.1. Voltage-time responses during oxidizing process

Figure 2 shows the variation of voltage during oxidizing process in baths with and without titania **nano-particles** at the defined waveforms (Table 2). The final voltages are 701 V for S1W1, 709 V for S1W2, 715 V for S1W3, 684 V for S2W1, 702 V for S2W2 and 708 V for S2W3. The difference between the voltage-time responses is negligible. This is also in agreement with our previous work [28]. However, it seems that the small differences exist between the final voltages are attributed to some different characteristics of the coatings especially the thickness. It is also found that the **nano-particles** have no noticeable effect on the voltage-time behavior at any operational conditions. Similar results were found by Lv et al. [34] in the case of graphite particles.

#### 3.2. Morphological observation

Figure 3 shows the surface morphology of the coatings. The specimen oxidized using unipolar waveform in silicate bath shows a complete pancake-like morphology which can be found in many references [35-37]. When the bipolar waveforms were used, the surface morphology changed to a combination of pancake and crater like. **By assuming complete pancake morphology for S1W1 and S2W1 (they also shows wide micropores), the crater/pancake ratios**

estimated by means of “Mipcloud image processing software” were estimated as 0.27, 0.56, 0.36 and 2.45 for S1W2, S1W3, S2W2 and S2W3, respectively. By increasing the cathodic duty cycle, the crater/pancake ratio and the size of the craters further increased.

Craters and **micro-pores** are both traces of **micro-discharges** in PEO coating of aluminum alloys. The craters are bumps which have irregular shallow holes in their **centers**. The holes in the center of these cratered regions suggest that they are formed as a result of strong **micro-discharges** [38]. The size of the craters reflects the strength of the **micro-discharges** and eruption of molten oxides during PEO process. On the other hand, the **micro-pores** are usually deep and surrounded by flat areas which may continue down to reach the substrate surface. Hence, they are more deteriorative for coating properties than the craters. The **micro-pores** are created from excessive gas liberating and escaping which are usually seen on the coating surface as regular circular holes. They are also usually created in the middle of discharge channels as they are the last solidified regions. For better understanding, some of the **micro-pores** are shown with arrows in Figure 3 d and some craters are also shown in Figure 3 f.

After solidification, the surface of PEO coatings usually consists of craters, some solidified pools around the craters, some **micro-pores** and even some **micro-cracks** resulted from the stresses [39]. By comparing the coatings morphologies, it is seen that the large craters are modified by adding  $\text{TiO}_2$  **nano-particles**, but wide **micro-pores** can be found at all the waveforms especially for the unipolar one. The density of **micro-cracks** on the surface of  $\text{Al}_2\text{O}_3/\text{TiO}_2$  composite coatings is obviously higher than on the  $\text{Al}_2\text{O}_3$  coating indicating a higher surface stress in the composite coatings. It is expected that the  $\text{Al}_2\text{O}_3/\text{TiO}_2$  composite coatings with higher **micro-cracks** density and wider **micro-pores** show the **weakest** corrosion resistances.

### 3.3. Coatings thickness measurements

The coatings thicknesses measured by eddy-current technique are presented in Figure 4. According to the obtained results, the thickness of both  $\text{Al}_2\text{O}_3$  and  $\text{Al}_2\text{O}_3/\text{TiO}_2$  composite coatings deposited using the bipolar waveforms has increased with respect to that produced using the unipolar waveform. A slight increase of thickness can also be considered by increasing the cathodic duty ratio, especially for the composite coatings. Using the unipolar waveform, the coating thickness is reduced by incorporation of titania **nano-particles**. It is in accordance with **ref. [22]** in which the thickness of the coating was reduced significantly when utilizing particle-containing electrolytes. The inert particles may be considered as obstacles for coating growth reducing the effective area for formation of conversion products which are finally converted by the discharges into the coating [16].

Figure 5 shows SEM cross-section images of the coatings. **Due to the nature of eddy-current thickness measurement which can be affected by roughness, porosity and etc., the thickness values obtained by SEM and eddy-current are not the same, but, the trend of variation is similar for both techniques. Additionally, it should be noticed that the cross-section images are focused on small zones of the coatings, while, the eddy-current considers wider area.** The compactness of the coatings is higher for the coatings produced by the bipolar waveforms. Also, the compactness seems to be increased by increasing the cathodic duty ratio as is seen in Figure 5c and f.

The cathodic current density can be adjusted by altering either cathodic duty cycle or cathodic voltage amplitude. For example, Li et al. [40] have reported that the same coating thickness can be achieved by increasing the cathodic voltage while the overall process time is reduced. At a constant overall process time in the present study, a higher thickness of oxide layer was found by increasing the cathodic duty ratio from 0 to 20 % and even higher when it increased to 40 %. It

seems that by selecting a proper pulse program, an improvement in coating quality is also possible. As is seen in Figure 5, the compactness of both  $\text{Al}_2\text{O}_3$  and  $\text{Al}_2\text{O}_3/\text{TiO}_2$  coatings is increased by increasing the cathodic duty ratio, in agreement with Yao et al. [41]. However, the coating thickness is also increased (Figure 4) in agreement with Li et al. [40], in contrary to Yao et al. [41]. It can be concluded that increasing the cathodic duty cycle will increase the thickness, but, the rate of this increase is not constant and reduces at higher duty cycles. This means that if the level of cathodic duty cycle is already high enough, its increase would not increase the coating thickness further or even shows a reverse effect due to reducing ingress of electrolyte constituents into the coating as can be found in the work of Yao et al. [41]. This is probably the reason for contradicting results obtained by different researchers. It seems that, due to the unique effect of cathodic cycles of the bipolar waveforms, the sites of succeeding anodic breakdowns are randomized and restricted to be occurred at localized sites. The repetition of breakdowns in the same locations leads to localized breakdown areas which promotes the formation of large discharge channels [7]. The larger discharge channels lead to a high porous and low adhered coating, which also promotes coating spallation during PEO process. Therefore, the coatings produced using DC [28] and unipolar waveforms, which provide no cathodic parts, are usually more porous. In contrary, using the bipolar waveforms leads to a higher compactness and also a higher thickness for both  $\text{Al}_2\text{O}_3$  and  $\text{Al}_2\text{O}_3/\text{TiO}_2$  composite coatings.

In the present study, a current density of  $5.6 \text{ A/dm}^2$  has been applied during PEO process. It is about one third of the DC magnitude used in our previous work (i.e.  $15 \text{ A/dm}^2$ ) [28]. However, it is found that the coatings become thicker than those produced using DC mode for the same oxidizing time period. This proves that the remarked differences observed on thickness of the coatings produced using DC and pulse waveforms are resulted by the mode of current not just its

net value. It seems that the oxidizing efficiency of pulse currents is noticeably higher than the corresponding DC one. Moreover, for the polar waveforms, the higher cathodic duty cycle shows a slight higher efficiency.

### 3.4. Coatings roughness measurements

The results of roughness measurements for  $\text{Al}_2\text{O}_3$  and  $\text{Al}_2\text{O}_3/\text{TiO}_2$  composite coatings are summarized in Table 3.

**Table 3: The average value of roughness (Ra) and the value between the highest peak and the deepest valley (Rz)**

	Ra ( $\mu\text{m}$ )	Rz ( $\mu\text{m}$ )
Aluminum substrate	0.079	1.915
S1W1	2.660	22.865
S1W2	3.113	28.129
S1W3	4.004	36.526
S2W1	3.607	33.650
S2W2	4.010	35.006
S2W3	5.153	35.972

As mentioned before, adding titania **nano-particles** has not led to a decrease of thickness for the coatings produced by the bipolar waveforms (Figure 4). However, the average roughness values (Ra) of S2W2 and S2W3 composite coatings are higher than corresponding S1W2 and S1W3 ones (Table 3). For the coatings produced using unipolar waveform, the thickness of S2W1 is lower than S1W1, but its roughness is higher. These findings suggest that the roughness of the coatings is not only depending on thickness. By reconsidering the morphological observations (Figure 3), it is seen that the crater size in the case of  $\text{Al}_2\text{O}_3/\text{TiO}_2$  composite coatings is smaller than corresponding  $\text{Al}_2\text{O}_3$  coatings. Thus, the higher roughness of the composite coatings can be related to their wider **micro-pores**. A similar result has been reported by adding graphite particles

[42]. It has been suggested that the motion of viscose electrolyte would be slower as the graphite is added, which enhances more ejected alumina to be suctioned out to the vacuum and enlarges the solidified pool during the PEO process. More viscose electrolyte **decreases** the weak points, **strengthens** the electrical field and **causes** more intense plasma discharging. The more intense plasma discharging provides a rougher surface, which describes why the oxide coating at the presence of graphite additive shows a rougher surface. In our study, the incorporation of **nano-particles** into the molten aluminum oxide is assumed to affect the melt viscosity too. As the higher surface roughness is related to the higher viscosity of the electrolyte bath or the molten oxide, the same conclusion may be made by adding titania **nano-particles**.

It can be seen from Table 3 that the higher cathodic duty cycle has also led to the higher Ra value for both  $\text{Al}_2\text{O}_3$  and  $\text{Al}_2\text{O}_3/\text{TiO}_2$  coatings. According to Li et al. [40], the coating which experiences a higher cathodic current density must reveal lower surface roughness because of the higher uniformity and compactness. However, this seems true for coatings with the same thickness. For a thicker and compacter coating, a higher energy is required for the current to pass through the oxide layer. Under this condition, the current will be localized at weak points of the layer to find its way across the coating. This is the reason why the diameter of the discharge channel increases with oxide thickness, and consequently, the larger **micro-pores** and higher surface roughness are obtained [1, 12, 38].

### **3.5. Coatings composition and phase analysis**

Figure 6 shows GAXRD results of the coatings at incident beam angles of 3, 5 and 10 °. The main phase of all coatings is  $\gamma$ -alumina, besides an amorphous background in most cases. However, in the case of coatings oxidized in the bath containing titania **nano-particles**, rutile in the coatings is also present. As is seen in Figure 6d, e and f, the peak intensities related to rutile

are the same and this reveals that the incorporation of titania **nano-particles** into the coating may not be affected by the applied waveforms. Thanks to vigorous stirring of the bath, the suspended particles have randomly entered the discharge channels or they could randomly stick to the melt pools, and thus, contributed in coating formation. Nearly, the same results have been obtained using DC mode [28]. Additionally, the patterns show that the incorporated TiO<sub>2</sub> **nano-particles** are in their original crystalline structure, i.e. rutile. Although, the incorporated TiO<sub>2</sub> particles can facilitate  $\alpha$  to  $\gamma$  alumina transformation [28], it seems that this incorporation has not affected the matrix composition of the coating which is mainly  $\gamma$ -alumina. If particles are incorporated without a reaction or no new phase formation, it is considered to be an inert incorporation. The other possibility is the reactive or partly reactive incorporation, when the particles melt through the high energy discharges and then react with other components from the electrolyte and the matrix. The melting point of the particles is one crucial factor to determine the incorporation mode [17, 18]. Thus, it **is** found that TiO<sub>2</sub> **nano-particles** are incorporated into the alumina matrix coating inertly. This is probably due to the lack of energy for melting the particles or phase transformation. During the PEO process, the molten alumina can react with silicate ions presented in the electrolyte bath and forms alumina-silicate phases such as mullite [5] or it may be transformed to  $\alpha$ -alumina. However, the transformation of  $\gamma$ -alumina to mullite or  $\alpha$ -alumina phases needs enough energy which should be provided by plasma during PEO process [43]. The absence of the peaks related to mullite or  $\alpha$ -alumina in the coatings produced in the present study indicates that the magnitude of the applied current density is not sufficient to support these phase transformations. Although for the pulse mode of waveforms, the current peak at each cycle is high enough, the cycles occur in a very low time period (i.e. 100  $\mu$ S), which shut down the **micro-discharges** quickly and let no phase transformation occur during the PEO process.

Usually, low thickness and high porosity of the coatings besides the low adsorption coefficients of coating elements for X-ray (aluminum and oxygen) are responsible for detecting the substrate peaks at high intensity [28]. Figure 6 shows that although the coatings are as thick as 40  $\mu\text{m}$ , the peaks of aluminum substrate can be seen clearly in all patterns obtained at 10  $^\circ$ . This phenomenon proves that although the penetration of X-ray, and thus, its diffraction from substrate should be decreased by higher coating thickness, the porosity and low adsorption coefficients of the coatings elemental constituents have played the major roles.

### 3.6. EDS analysis and elemental maps of the coatings

Figure 7 shows elemental mappings of Al, Si and O of the surface of S1W1 specimen around a trace of a discharge channel. Figure 8 shows almost the same condition for S2W1 specimen, with additional Ti distribution. Through these channels, the molten alumina has flowed out of the channel and rapidly solidified. At the same moment, anionic components such as  $\text{PO}_4^{3-}$  and  $\text{SiO}_3^{2-}$  enter the channels leaving the sharp and distinctly visible boundaries of different compositions around them [44]. It is believed that the edges of the solidified pools and the accumulated particles regions contain higher silica and aluminosilicate phases than those regions close to the center of discharge channels. The molten oxide travels a longer way during the ejection from discharge channels, which allows more ions and solid suspensions to be attached [42]. In this way, silicon is distributed at lower concentration near the craters or **micro-pores** (two main traces of discharge channels) as seen in Figure 7 and 8. Aluminum signals are stronger in the mouth of traces, right in the places where silicon signals are weaker. This phenomenon shows that the contribution of ions from the substrate ( $\text{Al}^{3+}$ ) and ions from the electrolyte (mostly  $\text{SiO}_3^{2-}$ ) are not uniform across the surface of the coatings. However, by focusing on Ti elemental map in Figure 8f, it can be found that except some small concentrated regions, the

titania **nano-particles** are embedded uniformly all over the surface. However, the concentrated regions are apparently located inside the **micro-pores** and the craters, which may not be cleaned efficiently by rinsing the specimens in water after the coating process.

EDS analysis of the coatings surfaces is presented in Table 4. It seems that the amount of incorporated titania **nano-particles** shows no dependency on the applied waveform. This is also confirmed previously by GAXRD analysis results.

**Table 4: Surface composition (at.%) of Al<sub>2</sub>O<sub>3</sub> and Al<sub>2</sub>O<sub>3</sub>/TiO<sub>2</sub> composite coatings determined using EDS analysis**

Coating	O	Na	Al	Si	K	Ti
S1W1	55	1.5	20.5	21	1.5	
S1W2	55	1.8	24	17.5	1	
S1W3	55	2.5	20	20	2	
S2W1	54	1.8	30	9.5	0.6	2.5
S2W2	55	1.7	24	17	1.2	1.7
S2W3	56	2.4	17.7	19	2.5	2.3

### 3.7. Corrosion behavior

#### 3.7.1. Potentiodynamic polarization measurements

Potentiodynamic polarization tests were employed to investigate the corrosion behavior of the coated specimens in 3.5 wt.% NaCl solution adjusted at pH 4 using hydrochloric acid. The corrosion behavior of the coatings after 1 h immersion was evaluated using potentiodynamic polarization technique and the plots are shown in Figure 9. Corrosion potential ( $E_{corr}$ ),  $i_{corr}$  and  $R_p$  parameters are extracted from the plots and summarized in Table 5.

As is seen in Table 5, adding titania **nano-particles** into the silicate bath has led to the increase of  $i_{corr}$  for the composite coatings as compared with corresponding Al<sub>2</sub>O<sub>3</sub> coatings. However, both Al<sub>2</sub>O<sub>3</sub> and Al<sub>2</sub>O<sub>3</sub>/TiO<sub>2</sub> coatings produced using bipolar waveforms at cathodic duty cycle of

40% (i.e. S1W3 and S2W3 coatings) provide the best corrosion resistances ( $\sim 3$  and  $5 \text{ nA cm}^{-2}$ , respectively). As mentioned before, the content of titania **nano-particles** in the coatings are nearly constant and not dependent on the applied waveforms, thus, the corrosion resistance of both  $\text{Al}_2\text{O}_3$  and  $\text{Al}_2\text{O}_3/\text{TiO}_2$  coatings should be improved by modification in thickness, compactness or surface morphology of the coatings. However, the thickness of S2W2 is about twice of S2W1, but their corrosion current densities and polarization resistances have not shown such a difference (Table 5). This suggests no linear relationship between thickness and corrosion performance of the coatings. Moreover, Dehnavi et al. [38] have reported that the surface morphology and coating **micro-structure** play more important roles in determining the corrosion resistance of PEO coatings than thickness and even phase composition. It has also been found that the porosity of PEO coatings plays a crucial role on protection efficiency of PEO coatings in the corrosive environment [31, 38, 45]. As is seen in Figure 9, a polarization behavior more similar to bare 7075 Al alloy can be observed for S2W1 coating, which is most probably due to its wide open **micro-pores** (Figure 3d). This confirms the effect of porosity on corrosion behavior of the coatings. It has been demonstrated that the PEO coatings allow permeation of aggressive solution via **micro-pores** into the coatings [45]. However, it is well known that the PEO coatings increase the corrosion resistance through decreasing the charge-carrier mobility at substrate/electrolyte interface [43]. In the current study, it is concluded that although the coatings thickness may be effective in determining corrosion behaviour, the porosity and surface morphology play more determinative effects.

As is seen in Table 5,  $E_{\text{corr}}$ ,  $R_p$  and  $\beta_a$  values for both  $\text{Al}_2\text{O}_3$  and  $\text{Al}_2\text{O}_3/\text{TiO}_2$  coatings are increasing when the applied waveforms are changed from unipolar to bipolar. The increase of  $R_p$ ,  $E_{\text{corr}}$  and  $\beta_a$  are all indicating a higher corrosion resistance. Accordingly, it is obvious that

increasing the cathodic part of the applied waveform increases the corrosion resistance in both Al<sub>2</sub>O<sub>3</sub> and Al<sub>2</sub>O<sub>3</sub>/TiO<sub>2</sub> composite coatings. However, the anodic behavior of Al<sub>2</sub>O<sub>3</sub> and Al<sub>2</sub>O<sub>3</sub>/TiO<sub>2</sub> composite coatings are essentially different. The Al<sub>2</sub>O<sub>3</sub> coatings show passive behaviors with high  $\beta_a$  values and breakdowns in their anodic branches which is assumed to be as the localized corrosion feature [5, 30]. But, considering the Al<sub>2</sub>O<sub>3</sub>/TiO<sub>2</sub> composites, active corrosion behavior can solely be found. The active corrosion in the presence of a thick oxide is not expected unless the penetration of aggressive ions into the coating through **micro-pores** and/or **micro-cracks**, induce intensive local corrosion current densities [46]. Thus, it can be concluded that under anodic polarization, the aggressive anions such as Cl<sup>-</sup> ions, have migrated via pores to reach the substrate, leading to corrosion attacks at some local areas on substrate. Therefore, it is reasonable that the coatings with wider pores show the lower corrosion resistance with respect to the others. It has been proved that a higher  $\beta_a$  is the sign of the thicker coating with more compact structure that may be advantageous for suppressing the Cl<sup>-</sup> transfer during polarization [30]. The  $\beta_a$  values of the specimens are increased by increasing cathodic duty cycle of applied bipolar waveform, indicating a higher thickness and/or compactness of the coating which provides more suppression of Cl<sup>-</sup> anions ingress.

**Table 5: The extracted corrosion parameters from the polarization plots in Fig. 8 using Tafel extrapolation method**

Sample	$i_{\text{corr}}$ (nA.cm <sup>-2</sup> )	$E_{\text{corr}}$ (mV) vs. SCE	Average Tafel slopes (mV.dec <sup>-1</sup> )		$R_p$ (MΩ.cm <sup>2</sup> )
			$\beta_a$	$\beta_c$	
7075 Al alloy	1682±77	-714±5	13.1±2.5	569±24	0.008±0.001
S1W1	10±0.8	-799±79	93±23	196±50	2.65±0.18
S1W2	7±0.6	-780±15	204±39	149±84	5.44±2.06
S1W3	3±0.7	-522±108	641±65	176±20	17.18±7.81
S2W1	12±0.9	-773±83	28±2	128±15	1.15±0.22
S2W2	9±0.3	-740±33	35±10	164±22	1.44±0.15
S2W3	5±1	-711±88	100±4	283±39	6.34±1.72

### 3.7.2. Electrochemical impedance spectroscopy

Anodic oxide coatings, either produced by conventional anodizing or plasma electrolytic oxidation, are composed of two layers. The layers include an inner compact layer (barrier layer in the case of conventional anodized coatings) and an outer porous layer. The inner compact layers are up to several micrometers thick and if they are assumed perfect (with no pores and defects like thin barrier layers in conventional anodized layers [47]), the relevant resistance in EIS readings will be infinite. Some researchers believe that through-pores naturally exist in PEO coatings, allowing the corrosive solutions to penetrate inside the coatings and reach the substrate. In common electrical equivalent models used for fitting EIS data, it has been assumed that the porosity is continued up to the substrate surface [38, 39]. Xiang et al. [45] believe that the corrosion resistance of PEO coatings depends strongly on the inner compact layer assumed to be in direct contact with metal surface. EIS plots of non-sealed PEO coatings represents the compact and porous layers as two capacitive loops [5, 30-33, 38, 48-52]. An additional capacitive loop is expected to be appeared in the sealed case or when an insulating outer layer exists [46, 53]. However, the corrosion attack can be occurred when the substrate is exposed to the penetrated aggressive solution, which shows an additional capacitive loop.

Figure 10-12 shows Nyquist and Bode-Phase plots of the coatings after 1 h to 16 weeks immersion in 3.5% wt. NaCl solution adjusted at pH 4. The Nyquist plots show two capacitive loops, the high-frequency loop reflects the outer porous layer response, while the low-frequency loop is the response of the inner compact layer [30]. Here, the best appropriate model for fitting the EIS data is considered as the most popular model containing two time constants as seen in Figure 13. In this electrical equivalent circuit, no time constant is considered corresponding to substrate corrosion, because, it is assumed that the corrosive medium has not yet entered the

interface of substrate and compact layer [44]. In this circuit,  $R_s$  is the uncompensated solution resistance which depends primarily on the geometry of the electrochemical cell and the conductivity of the test solution.  $R_{out}$  is the outer porous layer resistance,  $R_{in}$  is the inner compact layer resistance, and the constant phase elements of  $CPE_{out}$  and  $CPE_{in}$  are related to the non-ideal capacitive behavior of the outer and inner oxide layers, respectively. The determined impedance elements after 1 h immersion are summarized in Table 6.

**Table 6: Fitting results of EIS data for  $Al_2O_3$  and  $Al_2O_3/TiO_2$  composite coatings after 1 h immersion in 3.5% NaCl at pH 4.**

Specimen Code	Solution $R_s$ ( $\Omega.cm^2$ )	Porous outer layer			Inner compact layer		$R_{in}$ ( $M\Omega.cm^2$ )
		$CPE_{out}$		$R_{out}$ ( $k\Omega.cm^2$ )	$CPE_{in}$		
		T ( $\mu F.cm^2$ )	P		T ( $\mu F.cm^2$ )	P	
S1W1	5.6	0.00114	0.990	2.278	0.2446	0.744	1.966
S1W2	5.2	0.06296	0.717	22.259	0.1615	0.655	3.542
S1W3	5.6	0.28320	0.664	7.097	0.5293	0.687	13.680
S2W1	16.4	0.10480	0.865	174.570	2.9733	0.481	1.225
S2W2	9.7	0.25730	0.788	643.510	2.6610	0.562	1.951
S2W3	2.5	0.76650	0.622	4.172	0.0469	0.865	10.430

Theoretically, when there is no inductive element in an EC model, the polarization resistance derived from polarization tests should be equal to the sum of resistances extracted from impedance diagrams. In this way,  $R_p$  can be considered as the sum of  $R_{in}+R_{out}$  [38]. From Tables 5 and 6, it can be seen that the changes in  $R_p$  value are in the same trend with sum of  $R_{out}+R_{in}$ . Table 6 also shows that the  $R_{in}$  is significantly higher than  $R_{out}$  for all the coatings, and thus,  $R_{in}$  determines the overall corrosion behavior of the coatings. This finding is in a good agreement with the literature [5, 12, 46, 49, 54]. Also, incorporation of  $TiO_2$  nano-particles or applying different waveforms has not altered this fact.

The  $R_{in}$  values for S1W1, S1W2 and S1W3 coatings are 1.966, 3.542 and 13.680  $M\Omega cm^2$  (Table 6), respectively. The variation of  $R_{in}$  with waveform shows that it is increased by applying bipolar waveform and raised significantly by increasing the cathodic duty cycle. This is also in

agreement with  $R_p$  values which are about 2.6, 5.4 and 17.1  $M\Omega\text{ cm}^{-2}$  (Table 5), respectively. According to Table 6, the maximum  $R_{in}$  value is obtained at cathodic duty cycle of 40 % for both  $Al_2O_3$  and  $Al_2O_3/TiO_2$  composite coatings (i.e. S1W3 and S2W3 samples). In our previous work [28],  $TiO_2$  nano-particles were found beneficial for reducing porosity in the coatings produced by DC current. In the present study, such an improvement cannot be seen. However, according to the obtained results, the hypothesis of the effectiveness of cathodic duty cycle on reducing porosity and improving surface morphology of PEO coatings has been proved for both  $Al_2O_3$  and  $Al_2O_3/TiO_2$  coatings.

It is interesting that the  $R_{out}$  is at the highest value when the bipolar waveform with cathodic duty cycle of 20 % has been applied and it is decreased significantly when the cathodic duty cycle is increased to 40 %. It can be concluded that by using the bipolar waveform with the lower cathodic duty cycle (20 %), the coating thickness increases with respect to unipolar waveform, but most of the thickness can be considered for outer porous layer, and this is why higher  $R_{out}$  values are achieved (S1W2 and S2W2). In contrast, by using the bipolar waveform with the higher cathodic duty cycle (40 %), the coating thickness does not increase noticeably with respect to the bipolar waveform with the cathodic duty cycle of 20 %, but, the most of its thickness is occupied by inner compact layer which provides a higher  $R_{in}$ . For this reason, the corrosion protection mostly determined by  $R_{in}$  is at the highest level for the coatings produced using bipolar waveform at the higher cathodic duty cycle (40 %) (i.e. S1W3 and S2W3) as seen in Table 6. It is concluded that, although the oxidation process is driven by the anodic pulses, the positive effect of right selected cathodic pulse cycles cannot be ignored.

In general, a higher coating porosity means a higher real surface area, and hence, a higher capacitance [31]. Some authors believe that the capacitance value can be correlated with

thickness of the oxide layer, and thus, the lower value of the capacitance can be related to a thicker layer [55]. Noting the capacitance values in Table 6, obviously both CPEs ( $CPE_{in}$  and  $CPE_{out}$ ) of S2W1 composite coating are higher than those for S1W1 coating suggesting a higher porosity and a lower thickness for S2W1 composite coating in agreement with SEM observations, which also confirm the polarization resistances obtained using potentiodynamic polarization readings. The same conditions can be observed for S2W2 and S1W2 coatings, but, with a difference that the thickness of these two coatings is almost the same (Figure 4). This implies that the higher capacitance means just a higher porosity of the layer. On the other hand, the  $CPE_{in}$  of S2W3 coating is lower than that for S1W3, and accordingly, the highest corrosion resistance in long immersion times is obtained for this composite coating (Figure 14).

According to Figure 14, it can be understood how the deterioration of both  $Al_2O_3$  and  $Al_2O_3/TiO_2$  composite coatings is progressing in the long-term immersion tests. The deterioration is seen at the first hours of immersion as sudden drops of inner compact layer resistances, which are found evidently in the overall corrosion behavior of the coatings. In addition, although some increase in diameter of the capacitive loops can be found after certain times, the overall trend is a gradual decrease (lower values of polarization resistance) for most of the coatings. Furthermore, the decrease of the radius of the low-frequency loop suggests that the response of barrier layer becomes less. This phenomenon can be attributed to the penetration of electrolyte into the coating [44]. The starting time and level for this fluctuation are different for each coating. For instance, this increase for S2W1 coating occurs after 72 h and the level of increase is also high, so it has reached  $864 \text{ k}\Omega \text{ cm}^2$  after 5 weeks immersion.

The decrease of  $R_{out}$  and  $R_{in}$  versus time suggests that the corrosive solution has been penetrated into the oxide coating through the outer porous layer, via the open pores [48]. When it reached

the inner layer, either degrading corrosion protect-ability of the coatings [49, 54] or hydration of the coatings [49] can be occurred. However, the latter is responsible for increasing the resistances. This is called “*repairing mechanism*” [53]. The  $\text{Al}(\text{OH})_3$  precipitates form deposits of white pustules at mouth of the pores or cracks resulting a blocking effect [56]. This is more likely for the coatings with relatively small size defects which can easily be blocked [56]. Since, no inductive loops are observed in Nyquist plots of the coatings even after 16 weeks, it can be concluded that there is not enough ingress of chloride ions inside the coatings defects to cause localized corrosion [48, 51].

By following the variations of  $R_{in}$  in Figure 14, it is found that the increase of  $R_{in}$  due to the pore plugging is more common for  $\text{Al}_2\text{O}_3/\text{TiO}_2$  composite coatings than for  $\text{Al}_2\text{O}_3$  ones. Among the coatings, the S2W1 coating shows the highest increase in  $R_{in}$  during immersion, but it drops after a while and reaches the minimum value after 10 weeks immersion. In contrary, the amount and increasing rate of  $R_{in}$  for S2W3 coating is lower than S2W1, but it is stable even after 16 weeks immersion. This observation reveals that the resistance created for PEO coatings by the repairing mechanism is not endless, especially when the coating has larger open micro-pores. On the other hand, it is considerable that the coating resistance is mainly determined by the “*intrinsic resistance*” of the inner compact layer. The intrinsic resistance is the resistance which the coating reveals just after immersion, and not through pore plugging or repairing mechanism. The coatings intrinsic resistances can be considered as the resistance values measured after 1 h immersion tests (Table 6). Although, the increase of  $R_{in}$  by repairing mechanism provides a high protection at first, it does not last for longer times if the coating suffers from low intrinsic resistance. For the coatings produced using the bipolar waveform with the higher cathodic duty cycle (40 %) (i.e. S1W3 and S2W3), which provide inner compact layers with the lowest

porosities, and also the highest intrinsic resistances (Table 6), the increased values of  $R_{in}$  through the repairing mechanism are stable up to 16 weeks as seen in Figure 14. The S2W3 composite coating provided even higher corrosion protection at longer times in spite of its lower intrinsic resistance than S1W3. This means that the role of the **micro-pores** plugging is more intense for the S2W3 composite coating. As is seen in Figure 14, the  $R_{in}$  of S2W3 coating has increased during immersion and even **reaches** to its initial value after 16 weeks.

SEM images of the specimens immersed up to 16 weeks are presented in Figure 15. Comparing with as-received morphologies in Figure 3, the images from corroded surfaces show that the **micro-structure** has not undergone any major changes, but it seems that a slight dissolution has occurred at the **micro-pores** in agreement with the work of Liang et al. [49]. Furthermore, Xiang et al. have found that the surface of PEO coatings had no major changes after 72 h immersion in 0.5 M NaCl solution [45]. Even, they found that the decrease of pore numbers may be caused by small quantity of corrosion products which could block the pores on the coating surface [45]. This confirms the results obtained in this research and demonstrates that the repairing mechanism is occurred by direct converting oxide to hydroxide.

#### **4. Conclusions**

$Al_2O_3$  and  $Al_2O_3/TiO_2$  composite PEO coatings were fabricated on 7075 aluminum alloy using unipolar and bipolar waveforms in a silicate electrolyte bath. By altering current waveform from unipolar to bipolar, the surface morphology of both  $Al_2O_3$  and  $Al_2O_3/TiO_2$  were converted from pancake to crater like. Appearance and introducing the cathodic duty cycle could increase thickness, roughness, polarization resistance and long-term corrosion resistance of the coatings.

The results revealed that adding titania **nano-particles** modified the craters, and also caused wider **micro-pores** and more **micro-cracks** in the coatings, which can deteriorate corrosion protection of the coatings. However, it was found that the presence of titania **nano-particles** has a negligible effect on voltage-time response of the PEO process. XRD and EDS analysis proved the inert incorporation and uniform distribution of TiO<sub>2</sub> **nano-particles** in the coatings and independency of their concentration to the applied waveform.

It was also demonstrated that the **micro-pore** plugging is an effective repairing mechanism and could increase the corrosion resistance of PEO coatings. The highest intrinsic resistance of the inner layer in the coatings produced using bipolar waveform with cathodic duty cycle of 40 % **provided** the highest protection and due to the lower porosity, the repairing mechanism **was** effective during the whole immersion time providing excellent long-term corrosion protection. In this way, the composite coating showed even higher corrosion protection at longer times.

### **Acknowledgment**

Supports from Iran Nanotechnology Initiative Council and Isatis Nano Plating Co. are gratefully acknowledged.

### **References**

- [1] S. Stojadinovic, R. Vasilic, I. Belca, M. Petkovic, B. Kasalica, Z. Nedic, L. Zekovic, Corrosion Science, 52 (2010) 3258-3265.
- [2] M.R. Bayati, H.R. Zargar, A. Talimian, A. Ziaee, R. Molaei, Surface and Coatings Technology, 205 (2010) 2483-2489.

- [3] S.A. Karpushenkov, A.I. Kulak, G.L. Shchukin, A.L. Belanovich, Protection of Metals and Physical Chemistry of Surfaces, 46 (2010) 463–468.
- [4] X. ShiGang, L. Jun, S. LiXin, Key Engineering Materials, 512-515 (2012) 1082-1088.
- [5] V. Raj, M. Mubarak Ali, Journal of Materials Processing Technology, 209 (2009) 5341-5352.
- [6] S. Sarbishei, M.A. Faghihi Sani, M.R. Mohammadi, Vacuum, 108 (2014) 12-19.
- [7] S.P. Sah, E. Tsuji, Y. Aoki, H. Habazaki, Corrosion Science, 55 (2012) 90-96.
- [8] V. Shoaiei-Rad, M.R. Bayati, H.R. Zargar, J. Javadpour, F. Golestani-Fard, Materials Research Bulletin, 47 (2012) 1494-1499.
- [9] V. Dehnavi, X.Y. Liu, B.L. Luan, D.W. Shoesmith, S. Rohani, Surface and Coatings Technology, 251 (2014) 106-114.
- [10] Y.-l. Cheng, M.-k. Mao, J.-h. Cao, Z.-m. Peng, Electrochimica Acta, 138 (2014) 417-429.
- [11] C.B. Wei, X.B. Tian, S.Q. Yang, X.B. Wang, R.K.Y. Fu, P.K. Chu, Surface and Coatings Technology, 201 (2007) 5021-5024.
- [12] J.B. Bajat, R. Vasilić, S. Stojadinović, V. Mišković-Stankovic, Corrosion, 69 (2013) 693-702.
- [13] Y.-l. Cheng, Z.-g. Xue, Q. Wang, X.-Q. Wu, E. Matykina, P. Skeldon, G.E. Thompson, Electrochimica Acta, 107 (2013) 358-378.
- [14] X. ShiGang, L. Jun, S. LiXin, Key Engineering Materials, 537 (2013) 76-81.
- [15] A.L. Yerokhin, A. Shatrov, V. Samsonov, P. Shashkov, A. Pilkington, A. Leyland, A. Matthews, Surface and Coatings Technology, 199 (2005) 150-157.
- [16] X. Lu, C. Blawert, N. Scharnagl, K.U. Kainer, Journal of Magnesium and Alloys, 1 (2013) 267-274.
- [17] X. Lu, C. Blawert, M.L. Zheludkevich, K.U. Kainer, Corrosion Science, 101 (2015) 201-207.
- [18] X. Lu, C. Blawert, Y. Huang, H. Ovri, M.L. Zheludkevich, K.U. Kainer, Electrochimica Acta, 187 (2016) 20-33.
- [19] X. Lu, C. Blawert, K.U. Kainer, M.L. Zheludkevich, Electrochimica Acta, 196 (2016) 680-691.
- [20] X. Lu, C. Blawert, M. Mohedano, N. Scharnagl, M.L. Zheludkevich, K.U. Kainer, Surface and Coatings Technology, 289 (2016) 179-185.

- [21] X. Lu, S.P. Sah, N. Scharnagl, M. Störmer, M. Starykevich, M. Mohedano, C. Blawert, M.L. Zheludkevich, K.U. Kainer, *Surface and Coatings Technology*, 269 (2015) 155-169.
- [22] X. Lu, M. Schieda, C. Blawert, K.U. Kainer, M.L. Zheludkevich, *Surface and Coatings Technology*, 307, Part A (2016) 287-291.
- [23] M. Mu, J. Liang, X. Zhou, Q. Xiao, *Surface and Coatings Technology*, 214 (2013) 124-130.
- [24] J. Liang, P.B. Srinivasan, C. Blawert, W. Dietzel, *Corrosion Science*, 52 (2010) 540-547.
- [25] A. Mandelli, M. Bestetti, A. Da Forno, N. Lecis, S.P. Trasatti, M. Trueba, *Surface and Coatings Technology*, 205 (2011) 4459-4465.
- [26] H.-m. Bian, Y. Yang, Y. Wang, W. Tian, *Powder Technology*, 219 (2012) 257-263.
- [27] H.-x. Li, R.-g. Song, Z.-g. Ji, *Transactions of Nonferrous Metals Society of China*, 23 (2013) 406-411.
- [28] A. Bahramian, K. Raeissi, A. Hakimizad, *Applied Surface Science*, 351 (2015) 13-26.
- [29] R.H.U. Khan, A.L. Yerokhin, A. Matthews, *Philosophical Magazine*, 6 (2008) 795–807.
- [30] H. Duan, C. Yan, F. Wang, *Electrochimica Acta*, 52 (2007) 3785-3793.
- [31] D. Sreekanth, N. Rameshbabu, K. Venkateswarlu, C. Subrahmanyam, L. Rama Krishna, K. Prasad Rao, *Surface and Coatings Technology*, 222 (2013) 31-37.
- [32] B. Yoo, K.R. Shin, D.Y. Hwang, D.H. Lee, D.H. Shin, *Applied Surface Science*, 256 (2010) 6667-6672.
- [33] M. Montazeri, C. Dehghanian, M. Shokouhfar, A. Baradaran, *Applied Surface Science*, 257 (2011) 7268-7275.
- [34] G.H. Lv, H. Chen, W.C. Gu, W.R. Feng, L. Li, E.W. Niu, X.H. Zhang, S.Z. Yang, *Current Applied Physics*, 9 (2009) 324-328.
- [35] E. Matykina, R. Arrabal, F. Monfort, P. Skeldon, G.E. Thompson, *Applied Surface Science*, 255 (2008) 2830-2839.
- [36] X. Wu, W. Qin, Y. Guo, Z. Xie, *Applied Surface Science*, 254 (2008) 6395-6399.
- [37] Z. Wang, X. Nie, H. Hu, R.O. Hussein, *J. Vac. Sci. Technol. A Vac. Surf. Films*, 30 (2012).

- [38] V. Dehnavi, D.W. Shoesmith, B.L. Luan, M. Yari, X.Y. Liu, S. Rohani, *Materials Chemistry and Physics*, 161 (2015) 49-58.
- [39] A. Fattah-Alhosseini, M. Vakili-Azghandi, M.K. Keshavarz, *Acta Metallurgica Sinica (English Letters)*, 29 (2016) 274-281.
- [40] Q. Li, J. Liang, B. Liu, Z. Peng, Q. Wang, *Applied Surface Science*, 297 (2014) 176-181.
- [41] Z. Yao, Y. Xu, Z. Jiang, F. Wang, *Journal of Alloys and Compounds*, 488 (2009) 273-278.
- [42] K.-J. Ma, M.M.S. Al Bosta, W.-T. Wu, *Surface and Coatings Technology*.
- [43] W. Yang, B.-l. Jiang, H.-y. Shi, L.-y. Xian, *J. Cent. South Univ. Technol.*, 17 (2010) 223-227.
- [44] H. Fadaee, M. Javidi, *Journal of Alloys and Compounds*, 604 (2014) 36-42.
- [45] N. Xiang, R.G. Song, H. Li, C. Wang, Q.Z. Mao, Y. Xiong, *Journal of Materials Engineering and Performance*, 24 (2015) 5022-5031.
- [46] Z. Li, X. Jing, Y. Yuan, M. Zhang, *Corrosion Science*, 63 (2012) 358-366.
- [47] A. Hakimizad, K. Raeissi, F. Ashrafizadeh, *Surface and Coatings Technology*, 206 (2012) 4628-4633.
- [48] P. Bala Srinivasan, J. Liang, R.G. Balajee, C. Blawert, M. Störmer, W. Dietzel, *Applied Surface Science*, 256 (2010) 3928-3935.
- [49] J. Liang, P.B. Srinivasan, C. Blawert, M. Störmer, W. Dietzel, *Electrochimica Acta*, 54 (2009) 3842-3850.
- [50] L. Wen, Y. Wang, Y. Zhou, J.-H. Ouyang, L. Guo, D. Jia, *Corrosion Science*, 52 (2010) 2687-2696.
- [51] A. Venugopal, R. Panda, S. Manwatkar, K. Sreekumar, L.R. Krishna, G. Sundararajan, *Transactions of Nonferrous Metals Society of China*, 22 (2012) 700-710.
- [52] M. Shokouhfar, C. Dehghanian, M. Montazeri, A. Baradaran, *Applied Surface Science*, 258 (2012) 2416-2423.
- [53] L. Wen, Y.M. Wang, Y. Liu, Y. Zhou, L.X. Guo, J.H. Ouyang, D.C. Jia, *Corrosion Science*, 53 (2011) 618-623.

[54] N. Xiang, R.-g. Song, J.-j. Zhuang, R.-x. Song, X.-y. Lu, X.-p. Su, Transactions of Nonferrous Metals Society of China, 26 (2016) 806-813.

[55] L. Pezzato, K. Brunelli, M. Dabalà, Surface and Interface Analysis, 48 (2016) 729-738.

[56] C. Liu, P. Liu, Z. Huang, Q. Yan, R. Guo, D. Li, G. Jiang, D. Shen, Surface and Coatings Technology, 286 (2016) 223-230.

## Figure captions

Figure 1: Oscilloscope recorded waveforms used for coating the specimens, a) W1, b) W2 and c) W3

Figure 2: Voltage- time responses for the specimens oxidized with conditions of Table 2. Maximum of voltages are recorded in specific times and represented as graphs.

Figure 3: Surface morphology of  $\text{Al}_2\text{O}_3$  and  $\text{Al}_2\text{O}_3/\text{TiO}_2$  composite coatings produced using unipolar and bipolar waveforms: a) S1W1, b) S1W2, c) S1W3, d) S2W1, e) S2W2 and f) S2W3

Figure 4: Thickness values of  $\text{Al}_2\text{O}_3$  and  $\text{Al}_2\text{O}_3/\text{TiO}_2$  composite coatings

Figure 5: SEM cross-section images of  $\text{Al}_2\text{O}_3$  and  $\text{Al}_2\text{O}_3/\text{TiO}_2$  composite coatings produced using unipolar and bipolar waveforms: a) S1W1, b) S1W2, c) S1W3, d) S2W1, e) S2W2 and f) S2W3

Figure 6: XRD patterns of  $\text{Al}_2\text{O}_3$  and  $\text{Al}_2\text{O}_3/\text{TiO}_2$  composite coatings produced using unipolar and bipolar waveforms: a) S1W1, b) S1W2, c) S1W3, d) S2W1, e) S2W2 and f) S2W3

Figure 7: Elemental map on the surface of S1W1 specimen around a trace of discharge channel.

Figure 8: Surface elemental map around a trace of discharge channel on S2W1 specimen.

Figure 9: Potentiodynamic polarization plots for the coated specimens and 7075 aluminum alloy substrate as the reference. The tests are performed in 3.5% NaCl solution at pH 4 after 1 h immersion at  $1 \text{ mV S}^{-1}$ .

Figure 10: a) Nyquist plots of PEO coatings after 1 h immersion in 3.5% NaCl at pH and an inset of the plots with maximum  $Z'$  and  $Z''$  of  $1 \text{ M}\Omega \text{ cm}^2$  b) Bode-Phase diagrams of the related plots

Figure 11: a) Nyquist plots of the PEO coatings after 4 weeks immersion in 3.5% NaCl adjusted at pH 4 with an inset of the plots with maximum  $Z'$  and  $Z''$  of  $50 \text{ k}\Omega \text{ cm}^2$ , b) Bode-Phase diagrams of the related plots

Figure 12: a) Nyquist plots of the PEO coatings after 16 weeks immersion in 3.5% NaCl adjusted at pH 4 with an inset of the plots with maximum  $Z'$  and  $Z''$  of  $50 \text{ k}\Omega \text{ cm}^2$ , b) Bode-Phase diagrams of the related plots

Figure 13: Equivalent electrical circuit used to fit the EIS data of PEO coated specimens,  $R_s$ : uncompensated solution resistance,  $R_{out}$ : outer porous layer resistance,  $CPE_{out}$ : constant phase element of outer porous layer,  $R_{in}$ : inner compact layer resistance and  $CPE_{in}$ : constant phase [5, 30-33, 38, 48-52]

Figure 14: The variation of  $R_{in}$  versus time for  $\text{Al}_2\text{O}_3$  and  $\text{Al}_2\text{O}_3/\text{TiO}_2$  composite coatings during immersion in 3.5 wt.% NaCl solution at pH 4.

Figure 15: SEM images of the coated specimens after 16 weeks immersion time in 3.5 wt% NaCl with adjusted pH of 4. a) S1W1, b) S2W1, c) S1W2, d) S2W2, e) S1W3 and f) S2W3

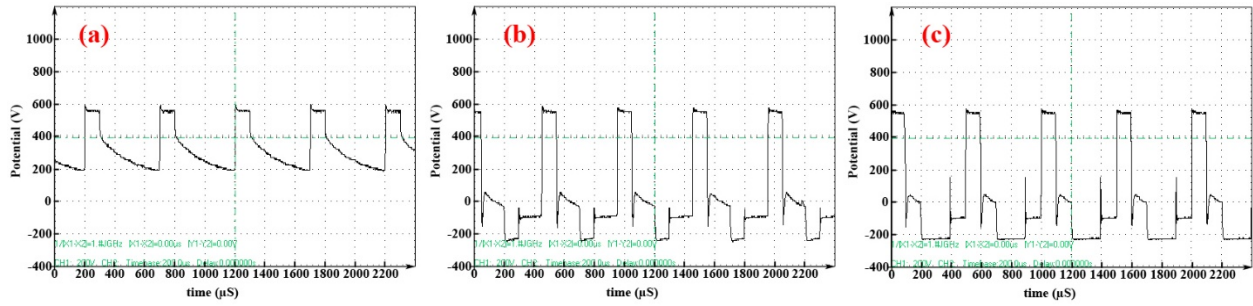


Fig 1.

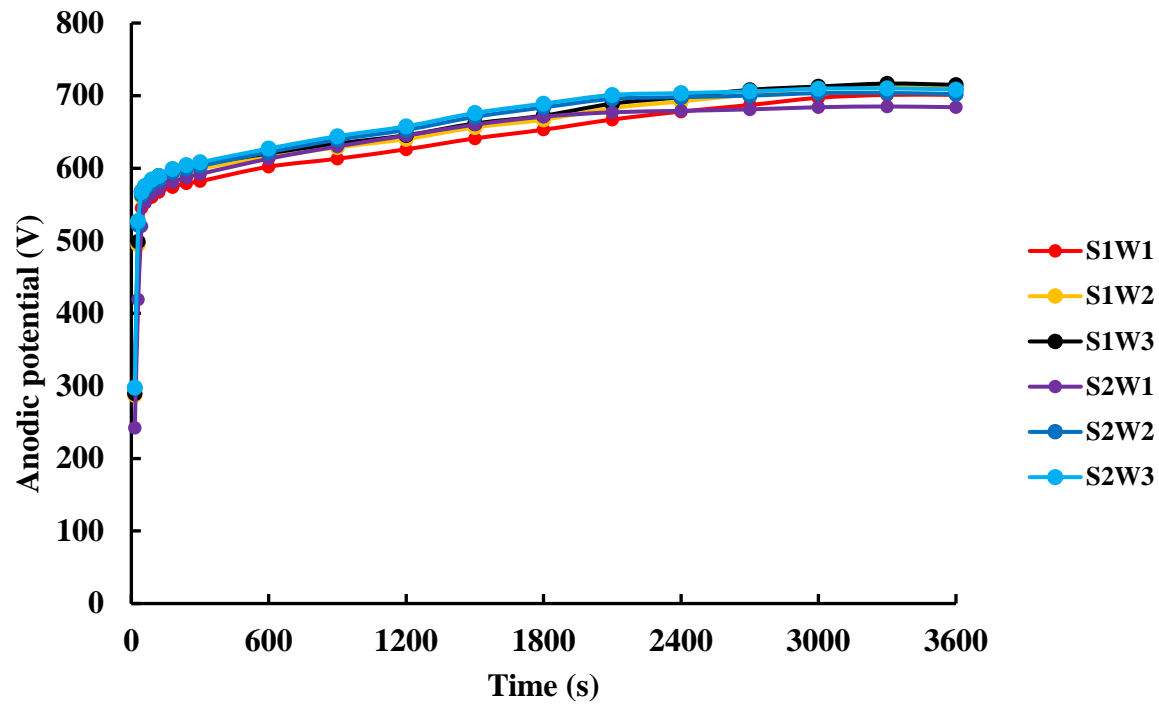


Fig 2.

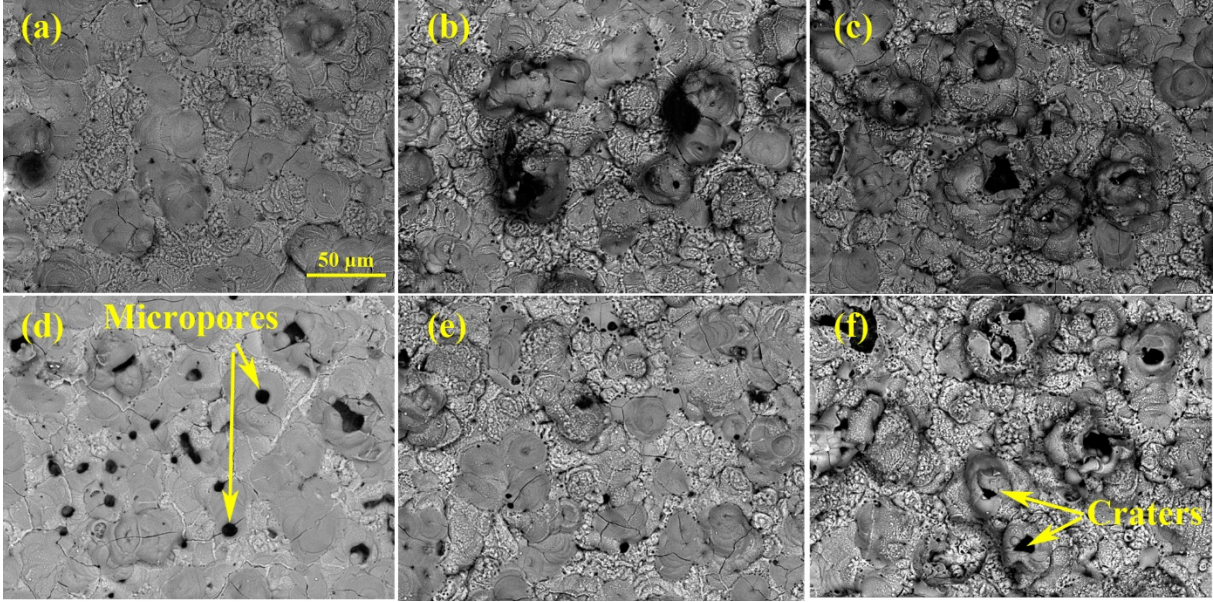


Fig 3.

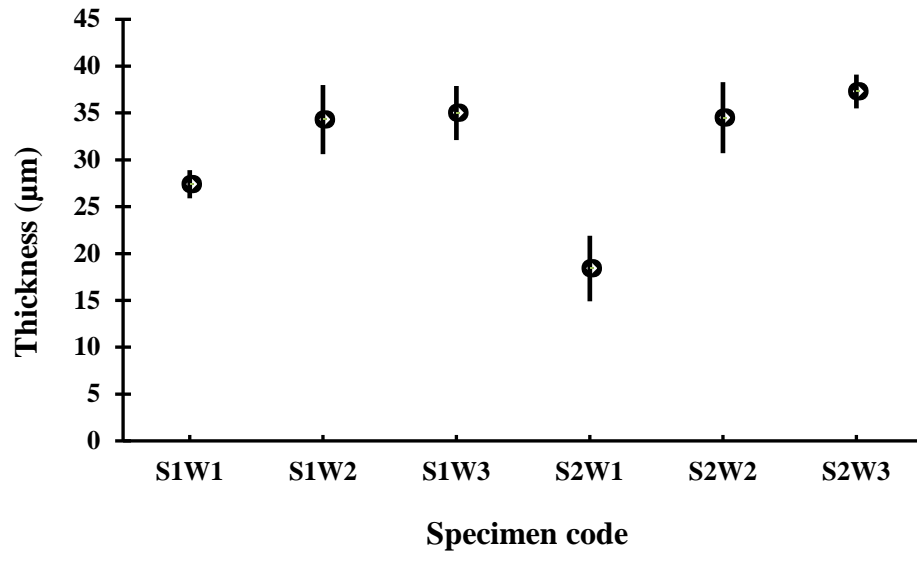


Fig 4.

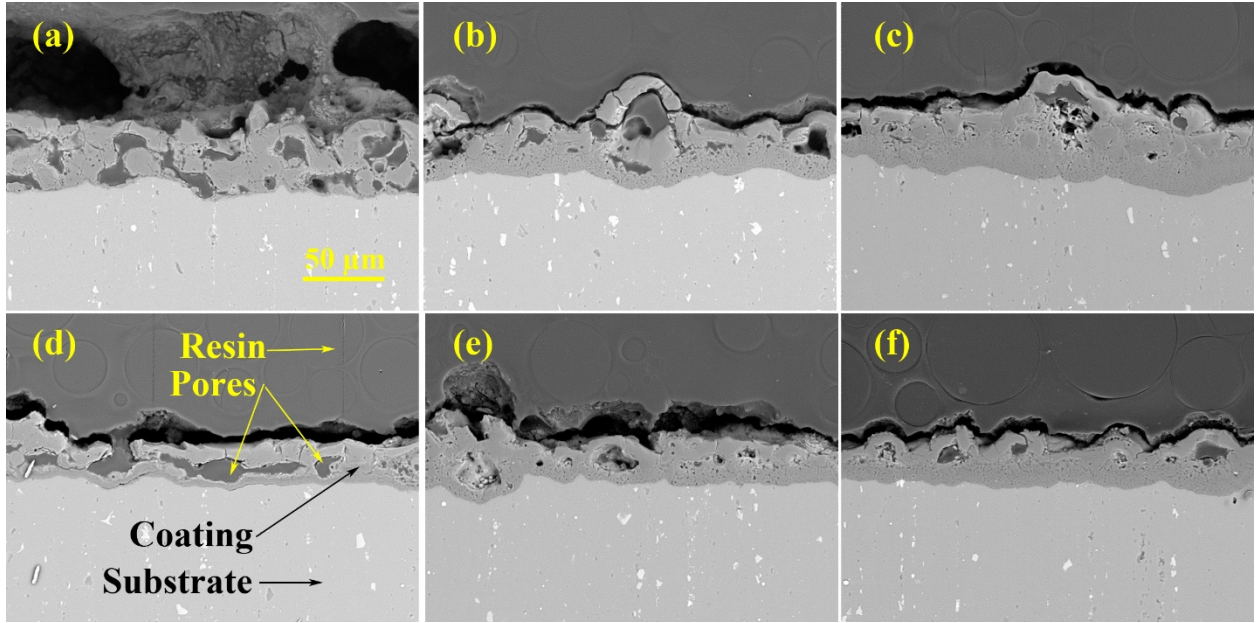


Fig 5.

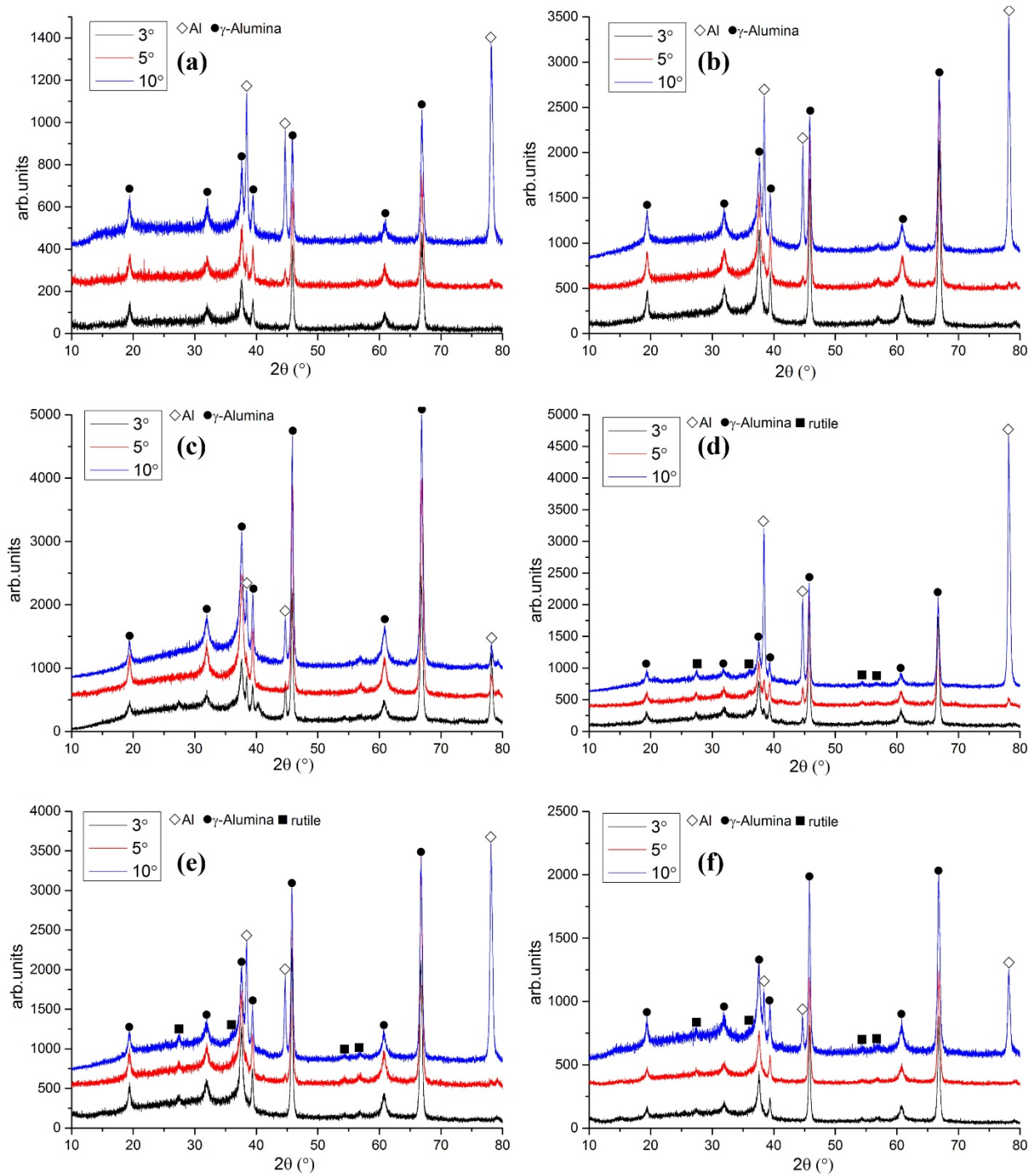


Fig 6.

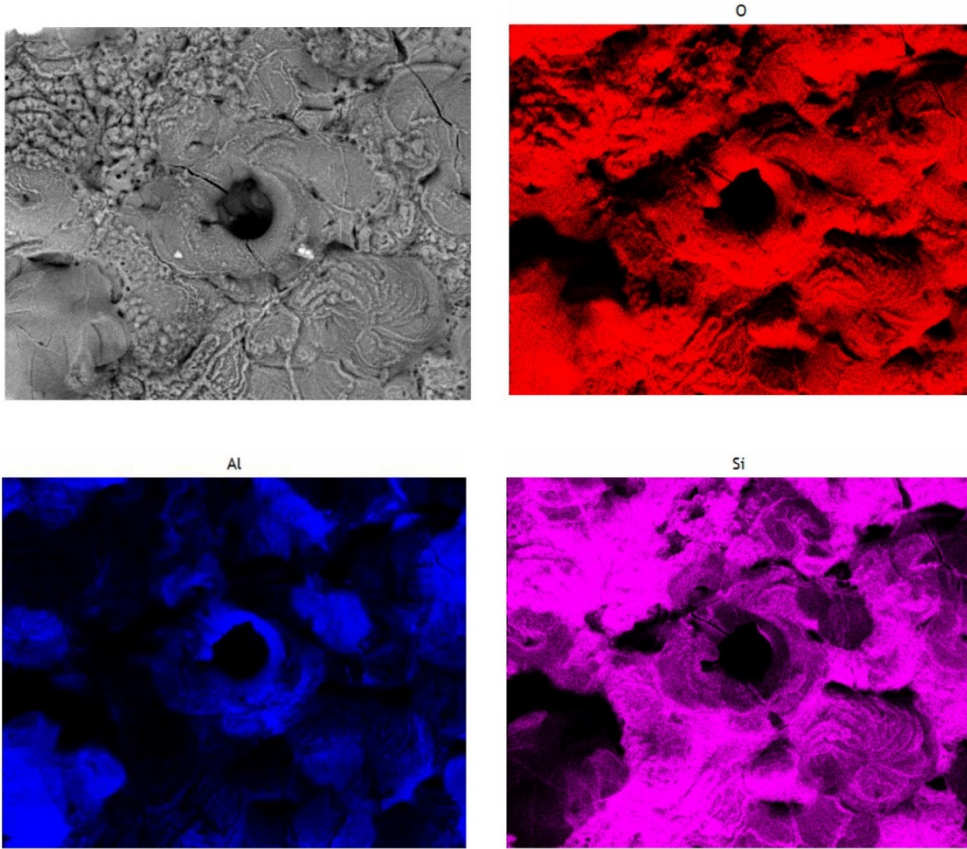


Fig 7.

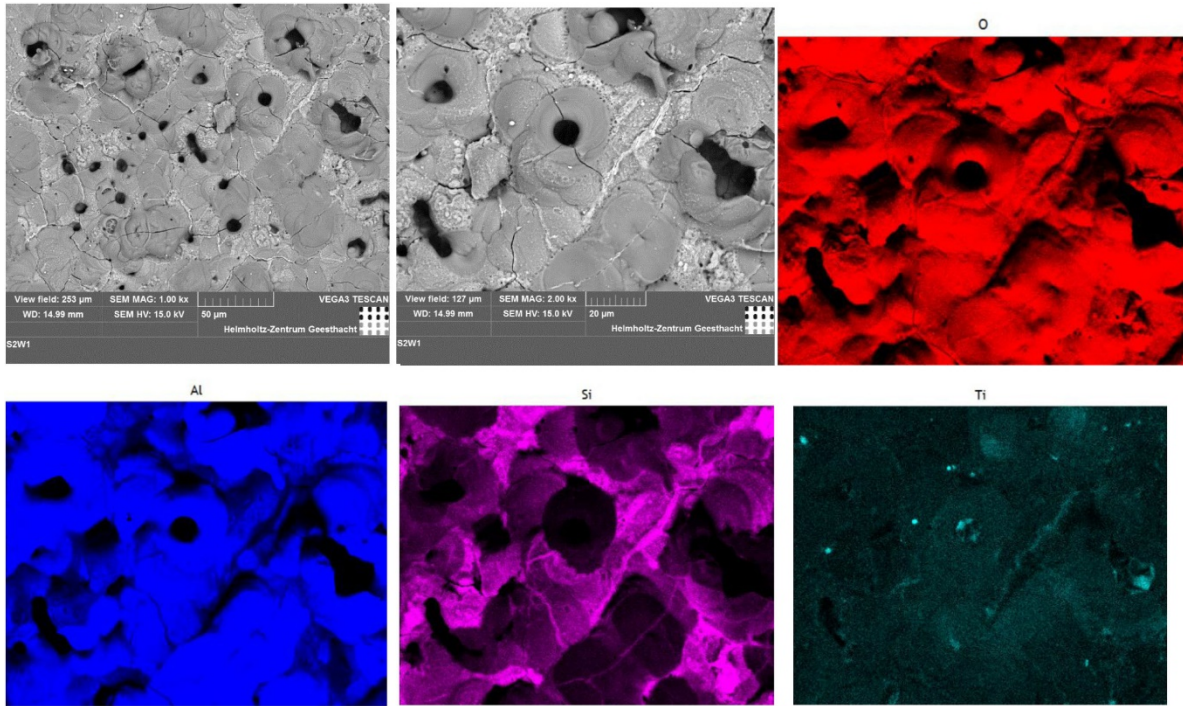


Fig 8.

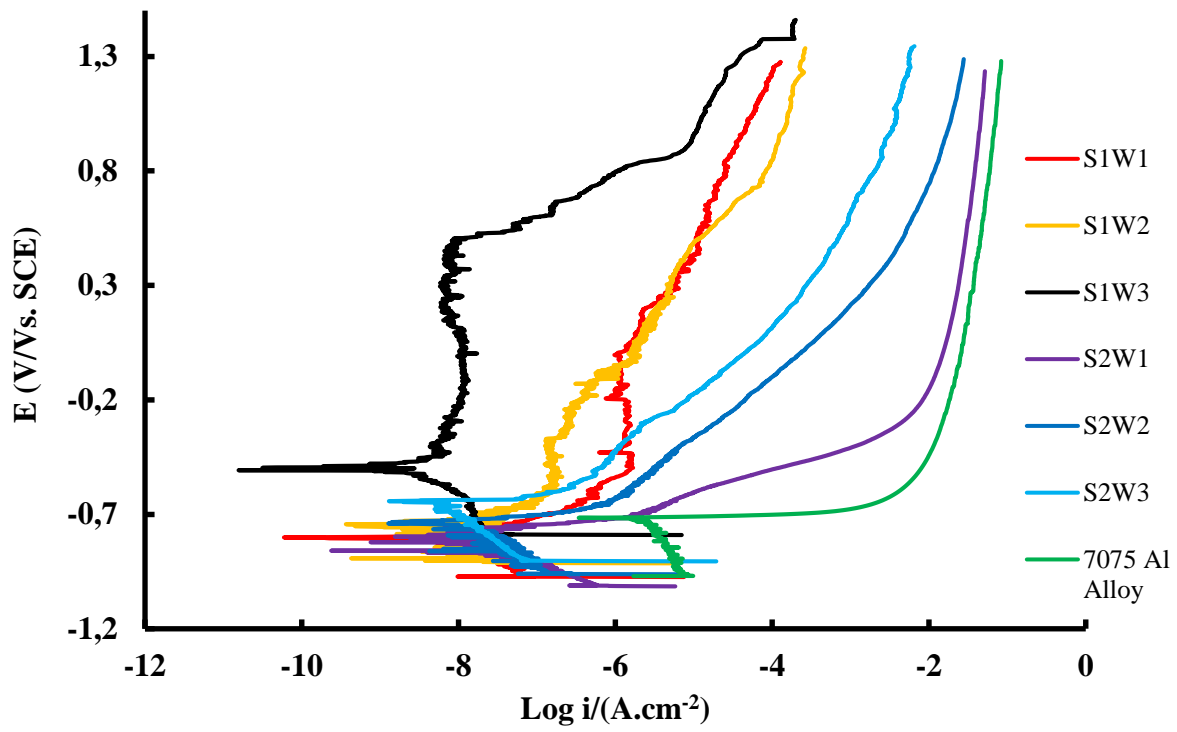


Fig 9.

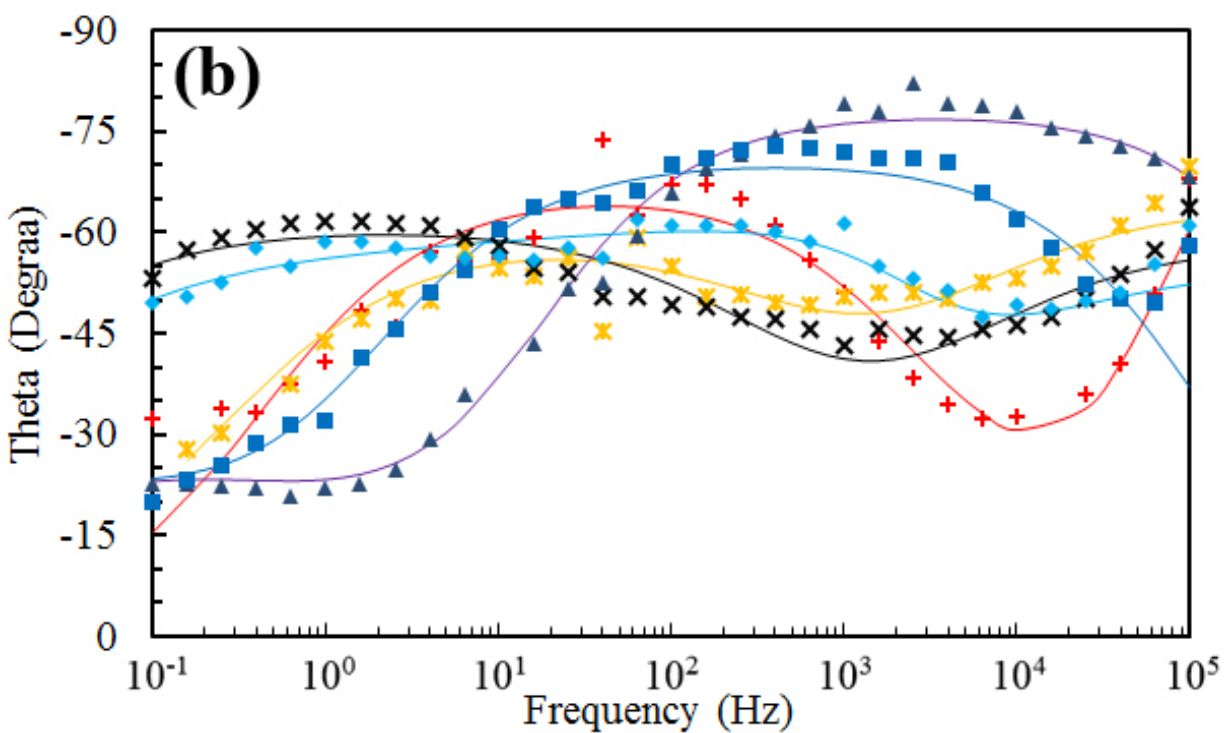
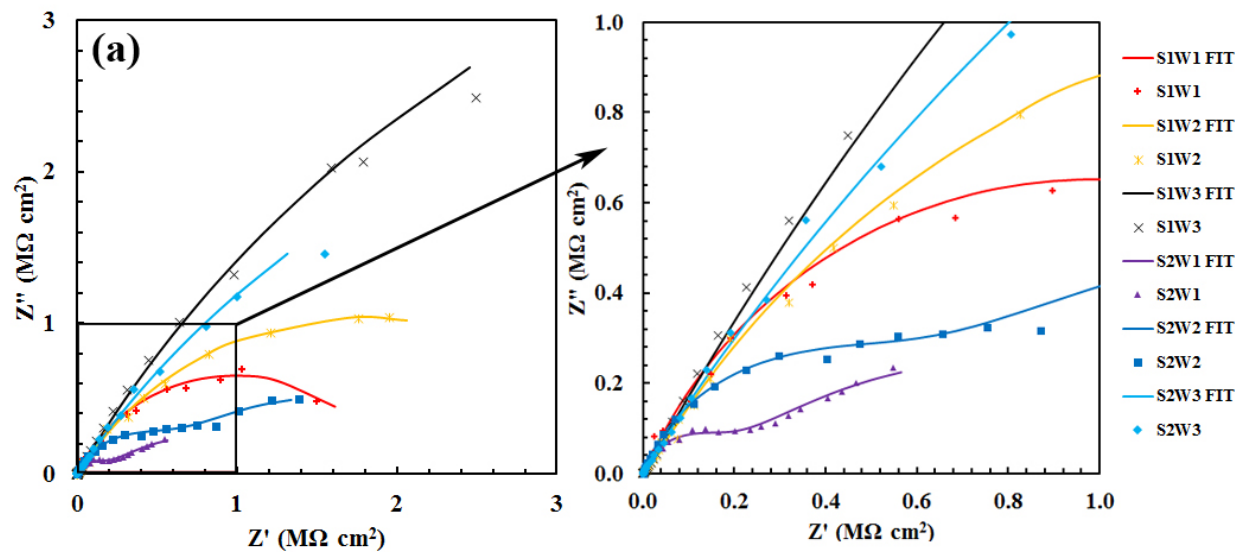


Fig 10.

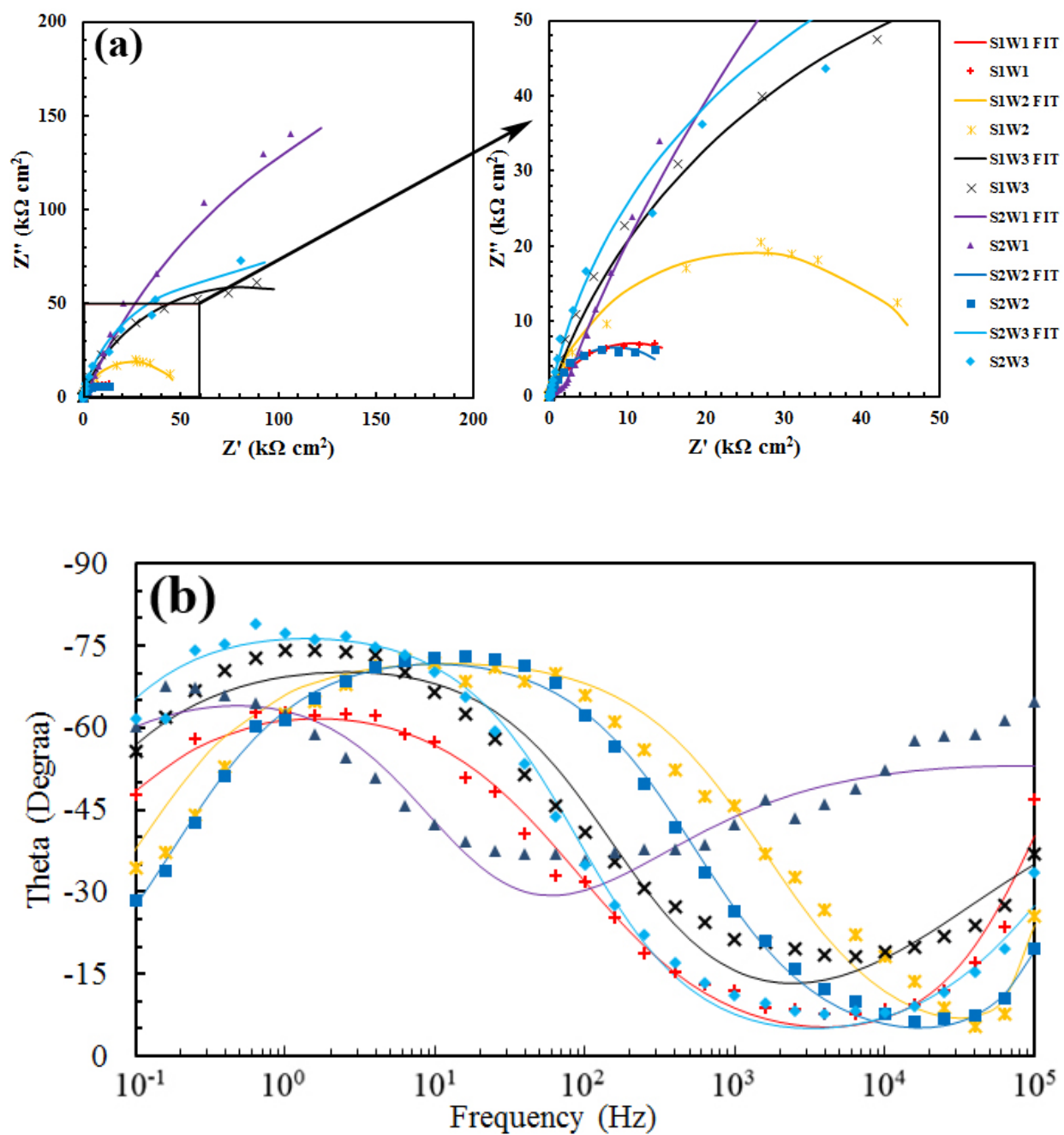


Fig 11.

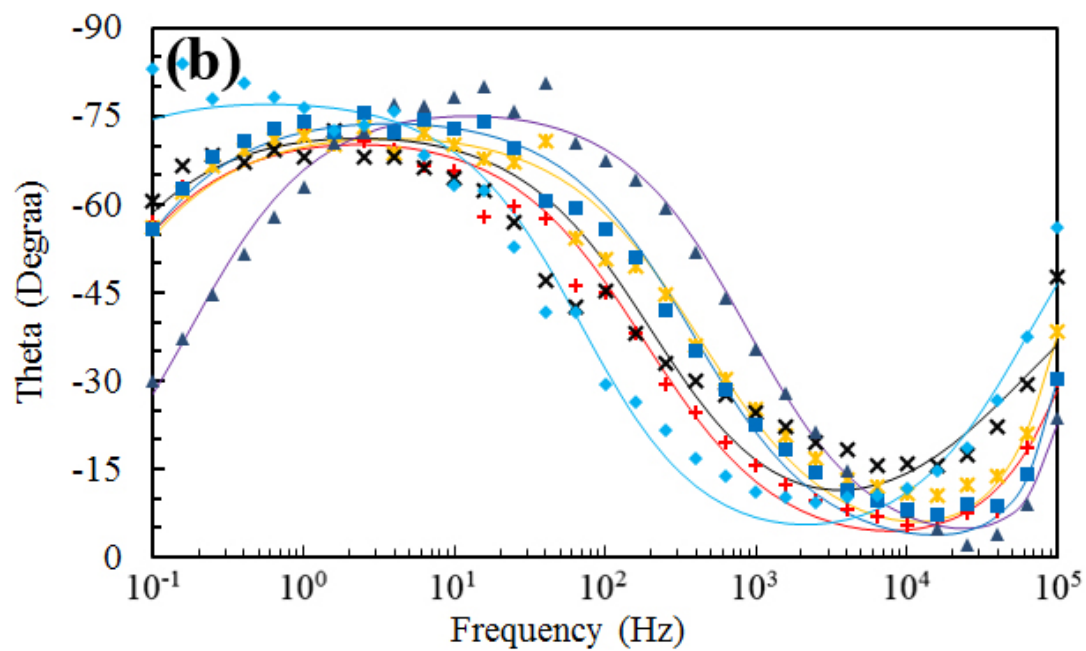
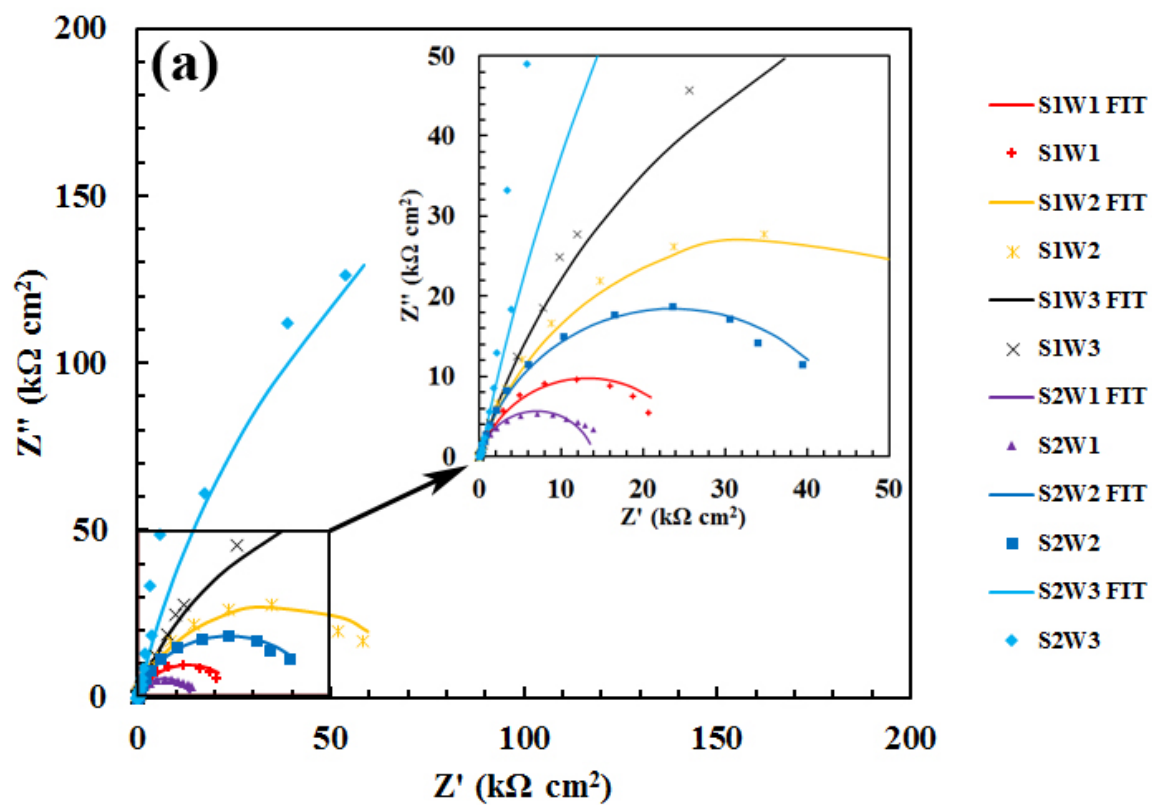


Fig 12.

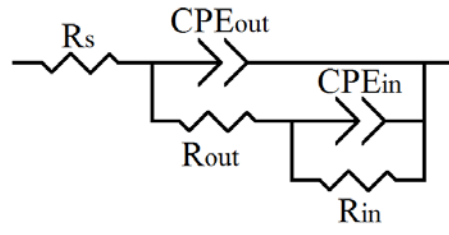


Fig 13.

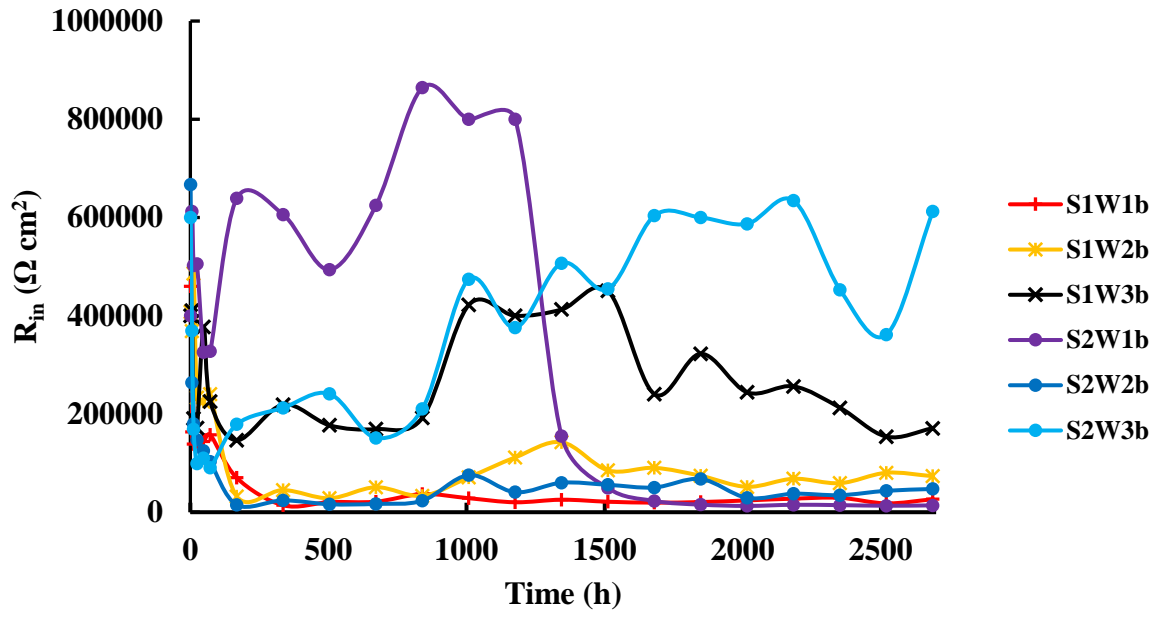


Fig 14.

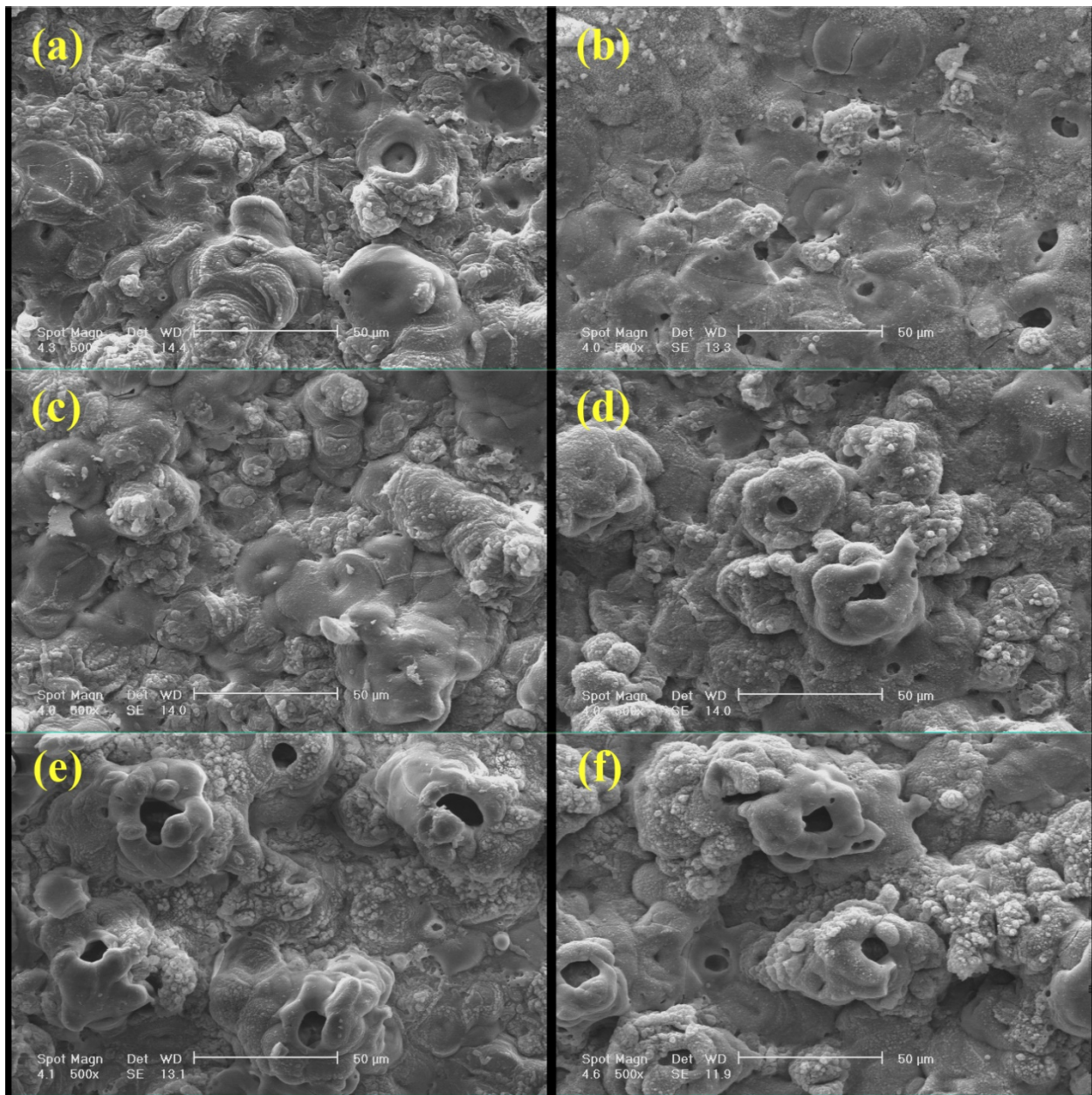


Fig 15.